Check for updates

Oxygen concentration measurement in 3D cell culture using multifocal optical projection microscopy

Birhanu Belay, †*[ac] Mart Kroon, †[bc] Kaisla Walls, [ac] Minna Kellomäki [bc] and Jari Hyttinen [ac]

Control over molecular oxygen concentrations in cell cultures is vital for maintaining normal physiological functions and modelling pathological conditions. However, current approaches for measuring oxygen are often invasive or limited in their capability to assess oxygen distribution in large-volume 3D cell cultures beyond a few hundred microns in depth. In this work, we have developed an adaptable method utilizing multifocal optical projection microscopy and commercially available fluorescent microsensor beads. Fluorescent projection images of the beads were acquired while simultaneously measuring oxygen concentration with an optical fibre-based sensor. A Stern–Volmer calibration curve was then generated by depleting oxygen with sodium sulfite, allowing fluorescence intensity to be converted into oxygen concentration. The method was demonstrated to quantify oxygen concentrations at depths beyond typical 3D cell culture dimensions, up to 21 mm. Fibroblasts were cultured within agarose hydrogels at varying cell densities (200 000 to 700 000 cells per ml). The results revealed a significant decrease in oxygen concentration with increasing cell density and depth of the specimen, thus also highlighting the need for O_2 measurements in 3D cell cultures. Here we demonstrated that our method is well suited for minimally invasive quantification of oxygen levels and gradients, especially in large-volume hydrogel-based 3D cell cultures.

1. Introduction

Advances in *in vitro* cell culture and engineered tissue models have highlighted the importance of controlling and monitoring the spatiotemporal distribution of key molecules. Among these, molecular oxygen (O_2) is vital for cell survival and mimicking *in vivo* conditions. Typical *in vitro* cell culture experiments are done in a 20% O_2 normoxic atmosphere, while the normal physiological or physioxic conditions in our tissues approximately range from 1.1% in the skin[1] to 13.5% in the alveoli.[2] Tumor tissues, which are known to exhibit a lack of oxygen, have concentrations ranging from 0.3% to 4.2%, whereas the corresponding healthy tissues range from 3.4 to 6.8%.[2] Mimicking different oxygen conditions is required not only for modelling healthy or tumor tissues, but also for trauma modelling, where the conditions are hypoxic as in cardiac ischemia[3] or ischemic stroke.[4] In this paper, we demonstrate

our three-dimensional (3D) cell culture measurement system and the need to measure oxygen concentrations within the cultures.

The transition from two-dimensional (2D) to 3D cell culture models has introduced challenges. As cells also consume oxygen, it is no longer uniformly distributed throughout the culture above critical cell densities.[5–9] Consequently, the oxygen availability within the 3D cell culture depends on factors such as the rate of cellular oxygen consumption, cell density, scaffold's diffusion properties, homogeneity, dimensions, and the availability of oxygen paths such as open-air channels. To address these limitations, various strategies have been proposed, including vascularization approaches,[10,11] implementation of different perfusion systems,[12,13] and modification of hydrogel properties.[6,14] However, the current availability for oxygen measuring methods for these systems remains limited.

Optical fibres with oxygen sensitive dye at the tip can provide accurate measurements in large samples. However, these probes are invasive and offer only pointwise measurements.[6,15–17] Additionally, integrating the probes into imaging and incubating setups can be challenging, and not well suited for closed-top organ-on-chip platforms. Several studies have demonstrated 2D measurements taken from the periphery of a 3D sample using oxygen sensitive films,[18,19] spots[20] and oxygen microsensor beads.[9,21] While these surface-based

[a]Computational Biophysics and Imaging Group, Faculty of Medicine and Health Technology, Tampere University, Tampere, Finland. E-mail: birhanu.belay@tuni.fi

[b]Biomaterials and Tissue Engineering Group, Faculty of Medicine and Health Technology, Tampere University, Tampere, Finland

[c]Centre of Excellence in Body-on-Chip Research, Faculty of Medicine and Health Technology, Tampere University, Tampere, Finland

† These authors contributed equally.

measurements provide valuable insight into oxygen concentrations and gradients, they lack direct measurements from within the interior of the 3D sample. A ratiometric method using custom-made microsensor beads has been developed for 3D cell cultures,[22] enabling localized oxygen measurements. However, the use of custom-made beads limits the method's accessibility. More recently, advanced imaging systems such as phosphorescence lifetime imaging microscopy (PLIM),[13,23,24] in combination with luminous beads, have been utilized for 3D oxygen mapping. Lifetime-based methods provide greater accuracy compared to intensity-based techniques, as they are inherently independent of dye concentration.[25,26] Nonetheless, PLIM imaging systems often require highly specialized and expensive instrumentation, posing a challenge to a broader adoption. Therefore, there remains a need for non-destructive, minimally invasive, and adaptable methods with imaging depth extending beyond several millimetres.

To address this, we developed a method to measure oxygen concentrations in 3D cell cultures using an optimized multifocal optical projection microscopy (MF-OPM) system.[27] MF-OPM enables imaging at different focal depths *via* applying an electric current to an electrically tunable lens (ETL), making it suitable for capturing fluorescence signals throughout the thick 3D culture. Oxygen sensitive fluorescent microsensor beads (CPOx-50-PtP) were embedded into the cell cultures and their fluorescence was imaged using MF-OPM. Local oxygen concentrations were quantified based on the oxygen-dependent quenching of the beads' signal. To demonstrate and validate the developed method, fibroblasts at varying cell densities were cultured to show the effect of cell density and depth on oxygen availability. These results revealed clear gradients with increasing cell density and imaging depth, indicating the applicability of the method for characterizing oxygen conditions in 3D cultures.

This paper presents a quantitative method to analyse oxygen concentrations in large-volume 3D hydrogel cell cultures. The method is based on MF-OPM and oxygen microsensor beads, enabling effective measurement of oxygen concentrations.

2. Materials and methods

2.1. Multifocal optical projection microscopy

The schematic of the in-house built MF-OPM setup is shown in Fig. 1. The MF-OPM imaging system is based on an electrically tunable lens (ETL) integrated into an optical projection tomography (OPT) setup for multifocal imaging. The more detailed description of the system can be found in our recent publications.[27,28] By remotely controlling the ETL, multifocal plane imaging can be achieved without moving the sample or the microscope objective lens. The multifocal images were acquired by applying varying current values into the ETL, ranging from 0 mA to 280 mA, with an interval of 5 mA. In all MF-OPM imaging experiments, the samples were prepared in a glass cuvette which was immersed in a larger cuvette filled with water (see zoomed-in view in Fig. 1). Images were acquired using a 5× infinity-corrected microscope objective with a numerical aperture (NA) of 0.14 and with an sCMOS camera

(ORCA-Flash 4.0, Hamamatsu, Japan). For brightfield imaging, a white light emitting diode (LED) (LED1 in Fig. 1) source was used to illuminate the sample. Epi-illumination was used for fluorescence imaging, with the sample illuminated using an LED (LED2 in Fig. 1). In all fluorescence imaging experiments using MF-OPM, an LED source at a constant power of 500 mV with 530/33 nm (M530L3, Thorlabs, USA) excitation wavelength and an emission bandpass filter of $\lambda = 716 \pm 40$ nm was used. The image size was 2048 × 2048 pixels, with an effective pixel size of 1.3 μm × 1.3 μm. The MF-OPM system is controlled using in-house-developed LabView-based (National Instruments, USA) image acquisition software.

2.2. CPOx-50-PtP microsensor bead photostability experiment

2.2.1 Sample preparation. To evaluate the photostability of the oxygen sensing microbeads (CPOx-50-PtP, Colibri Photonics, Germany) during the fluorescence imaging experiment, the samples were prepared by mixing 200 μl of bead solution (67 000 beads per ml in de-ionized H_2O) with 850 μl of gently microwave heated 1% agarose hydrogel (Sigma, USA). The sample was allowed to gelate at room temperature.

2.2.2 Imaging procedure. The photobleaching behaviour of the beads was characterized by measuring the fluorescence intensity of the beads for every 5 minutes for a total of 2 hours using the MF-OPM system. The images were captured with a 1-second exposure time.

2.2.3 Image analysis. Fiji software[29] was used for data analysis. Mean intensity from a 10 × 10 pixel area at the centre of each bead at a single focal plane was measured. The background signal intensity from the same plane was measured and subtracted from the bead intensities. The resulting mean intensity values were plotted with standard deviation.

2.3. CPOx-50-PtP microsensor bead fluorescence intensity calibration for oxygen measurements

2.3.1 Sample preparation. Samples were prepared by mixing 200 μl of bead solution (67 000 beads per ml in de-ionized H_2O) with 1000 μl of 1% liquid agarose, which was gently heated in a microwave oven. The mixture was placed in a glass cuvette, and a needle-type optical fibre oxygen microsensor (see Fig. 1) was inserted into the sample before the agarose gelated. The optical fibre's tip was positioned close to at least one oxygen sensitive bead, ensuring an accurate correlation between the measured oxygen concentration and the fluorescence intensity of the beads. The samples were then allowed to further gelate and stabilize for 24 h at room temperature before the measurement.

2.3.2 Imaging procedure and oxygen sensing. Before imaging, the sample was positioned so that both the bead(s) and the optical fibre tip were in focus. To deplete oxygen from the sample, 500 μl of a Na_2SO_3 solution (35 g/100 ml in de-ionized H_2O) was added on top of the hydrogel. Oxygen levels were simultaneously measured with the fibre-based sensor and imaged using MF-OPM. The fibre recorded oxygen concentration every 3 seconds, while fluorescence images were acquired
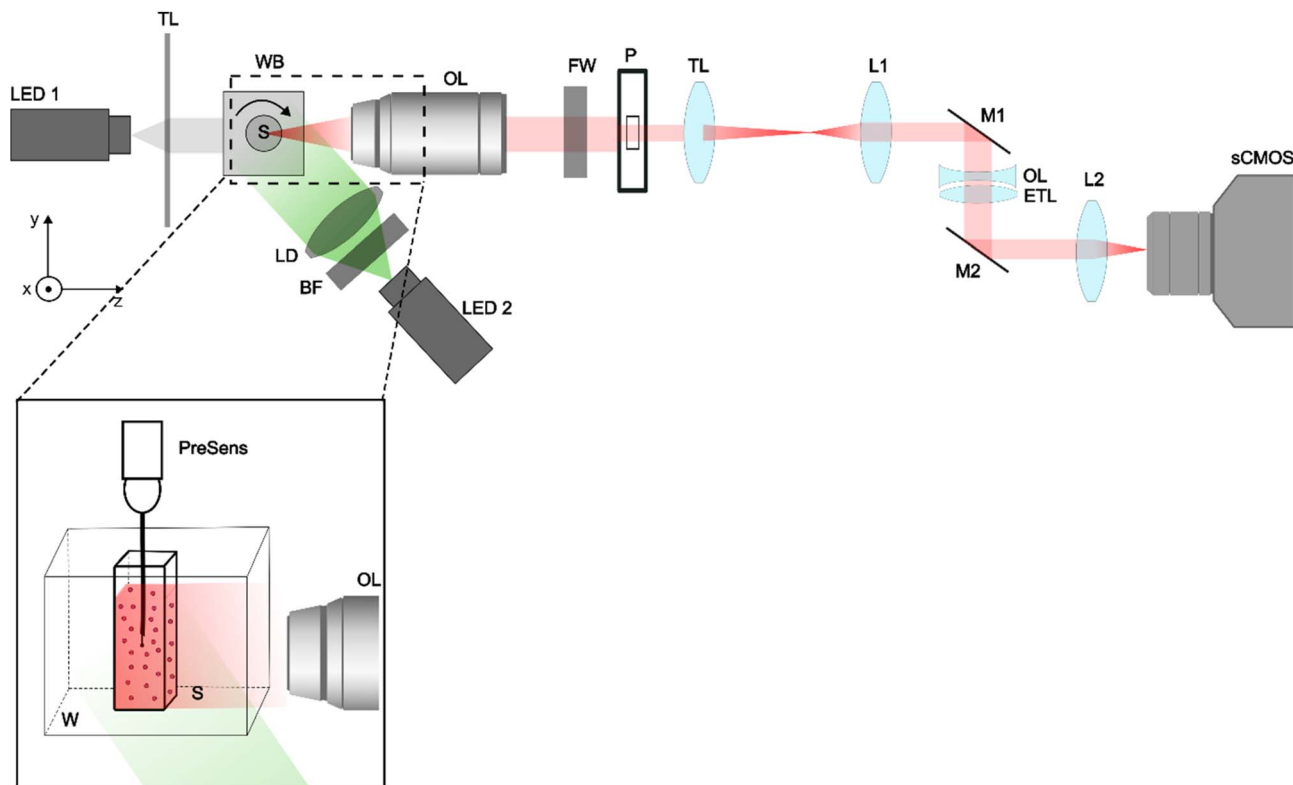
Fig. 1 A schematic of the MF–OPT setup. For label-free bright-field imaging, an LED (LED 1) with a telecentric lens (TL) is used to illuminate the sample, and the transmitted light is collected by an objective lens (OL). For fluorescence imaging, a second LED (LED 2) together with a bandpass filter and a light diffuser lens (LD) serves as the excitation source, and the backscattered fluorescence signal is collected by the same OL. Both transmitted and fluorescence signals pass through a filter wheel (FW) and a pinhole (P) and are then imaged using a tube lens (TL). The electrically tunable lens (ETL) system consists of a 4f configuration formed by two relay lenses (L1 and L2), an offset lens (OL), a remotely controlled ETL, and beam-steering mirrors (M1 and M2) that direct the beam in the vertical direction, which is finally imaged by an sCMOS camera. The zoomed-in schematic illustrates a hydrogel sample embedded with CPOx-50-PtP oxygen-sensing beads and an optical fibre oxygen probe (PM-PSt7, PreSens, Germany). The sample cuvette (S) is placed inside a larger water-filled glass cuvette (W).

at 1 frame per second with a 1-second exposure time. The experiment was performed at room temperature.

2.3.3 Image analysis. Oxygen sensing bead intensities were measured from the images with Fiji at 1% intervals, from 18% to 0% oxygen, to create the calibration curves. Mean intensities were calculated from 20-pixel diameter circular areas from each bead's centre. A linear fit was created by using the Stern–Volmer equation to obtain the variables a and b:

$$I_0/I = a + bx \tag{1}$$

where I_0: intensity at 0% oxygen, I: measured intensity and x: oxygen concentration. The linear curve was used to determine the O_2 level in 3D cell culture experiments.

2.4. CPOx-50-PtP microsensor bead cytocompatibility 2D cell culture

Cytocompatibility of the beads was evaluated using a Live/dead Viability Kit for mammalian cells (Invitrogen, USA) with Commercial WI-38 human lung fibroblasts at passage 22 (Culture Collections, Public Health England, UK). The cells were cultured for 2 weeks with the beads, and viability percentage was calculated after 4, 7 and 14 days of culture. The experiment is described in more detail in SI chapter S1.

2.5. Demonstration of oxygen measurement in 3D cell culture

2.5.1 CPOx-50-PtP microsensor bead sterilization. The beads were sterilized by incubating them in 100 μl of 70% ethanol for 1 hour. Ethanol was aspirated after centrifuging for 1 minute at 300g. To remove any ethanol residues, 1 ml of sterile phosphate buffer solution (PBS) was added. The suspensions were vortexed, followed by 1 minute centrifugation at 300g, after which the PBS was removed. Washing with PBS was repeated twice, and the beads were stored in sterile PBS at a concentration of 5 mg ml^{-1} (67 000 beads per ml). Prior to plating cells, PBS was aspirated after centrifuging and replaced with cell culture medium.

2.5.2 Cell culture. Commercial WI-38 human lung fibroblasts (passage 13) were used with the same materials as in the 2D cell cultures described in SI chapter S1. This robust cell line is commonly used in cytocompatibility testing and known for its highly proliferative behaviour, especially at passages under 30.[30] Three 3D cell culture samples were prepared at cell densities of

200 000 cells per ml, 400 000 cells per ml and 700 000 cells per ml in 1% agarose hydrogel mixed with sterilized sensor beads. Agarose hydrogels were used as a simple, inert, and non-adhesive 3D matrix for method development, enabling controlled and reproducible oxygen measurements independent of cell-matrix adhesion or matrix remodeling. For each sample, cells were suspended in 100 µl of pre-warmed (37 °C) culture medium. Separately, 20 µl of sensor beads, suspended in 37 °C medium at a concentration of 1 000 000 beads per ml, were mixed with the cell suspension by pipetting. Subsequently, 900 µl of liquid agarose hydrogel (37 °C) was added and thoroughly mixed with the cell-bead suspension. The resulting samples were transferred into glass cuvettes and incubated at 37 °C to allow the agarose to gelate. Once gelated, 500 µl of 37 °C medium was added on top of each sample. The final resulting hydrogel samples had dimensions of 8 mm × 5 mm × 25 mm (length × width × height). All the samples were incubated at 37 °C in 5% CO_2, and the medium was refreshed after 2 days, a few hours before imaging. Cell viability was studied in 3D cell cultures with the same live/dead assay used in the 2D cyto-compatibility experiment. The samples were visually inspected with the MF-OPM microscope and images were taken from the approximate centre of the 200 000 cells per ml and 700 000 cells per ml samples.

2.5.3 Imaging procedure. The MF-OPM and microsensor beads were used to measure oxygen levels at different depths within the 3D cell cultures. Imaging was performed with a 5× objective lens (NA = 0.14) and an sCMOS camera (2048 × 2048 pixels, 6.5 µm pixel size), resulting in a field of view of 2.66 mm × 2.66 mm. A motorized vertical stage was used to acquire eight image stacks along the vertical axis, extending up to ~21.3 mm below the sample surface. At each depth position, 280 focal planes were imaged, covering a range of ~700 µm in the middle of the sample. Bright-field images were also taken at each position prior to fluorescence imaging. All imaging was conducted at room temperature under ambient air conditions. To further ensure measurement consistency, all imaging parameters (excitation power, exposure time, and detector settings) were kept
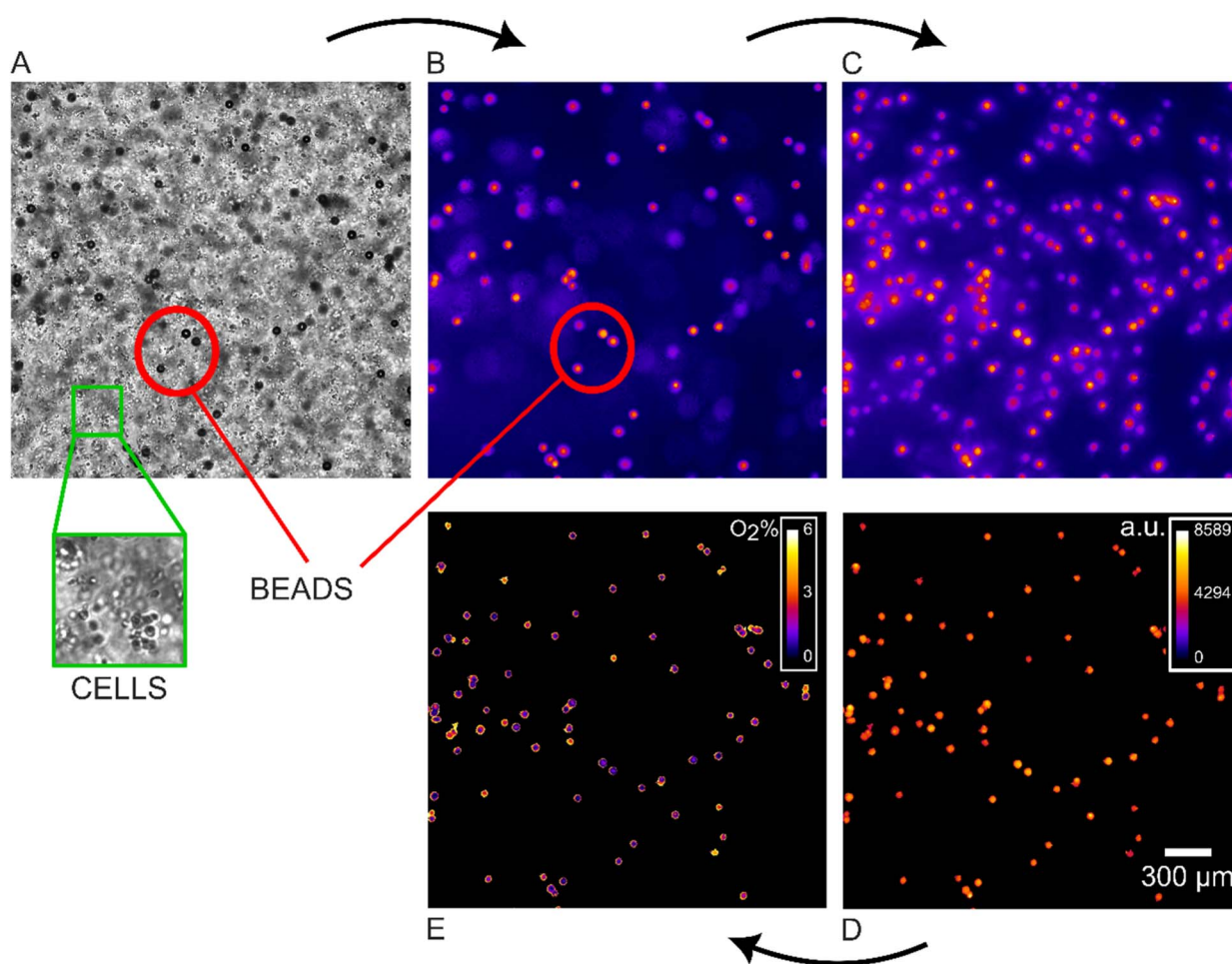

Fig. 2 A series of images demonstrating the image processing steps and conversion of intensity into an oxygen concentration map. The images are taken from a cell culture with 700 000 cells per ml, located ~20 mm below the surface. (A) Brightfield image from a single focal plane, showing both cells and beads, (B) fluorescence image from the same plane as A, (C) maximum intensity projection (MIP) generated from multifocal fluorescence imaging, (D) thresholded image from C after background subtraction, small size bead filtering, application of a high-intensity cutoff, and removal of small artefacts. (E) Oxygen concentration map generated from D using intensity to oxygen calibration. In D, fluorescence intensity (a.u.) is represented using the Fire LUT color bar.
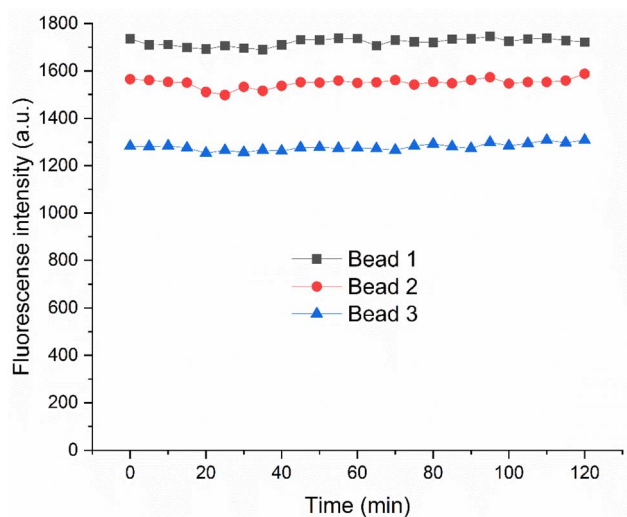
Fig. 3 Photobleaching experiment results for CPOx-50-PtP beads. No significant photobleaching behaviour was detected from the three measured beads.

constant throughout calibration and sample acquisition. This controlled acquisition workflow ensured that intensity-to-oxygen conversion remained valid across experiments and minimized variability introduced by instrumental factors.

2.5.4 Image processing and conversion of intensity to oxygen map. To quantify oxygen distribution within 3D cell cultures, fluorescence images were processed and converted into oxygen concentration maps using a step-by-step image analysis flow. For each lateral position in the sample, maximum intensity projection (MIP) images (Fig. 2C) were generated from the multifocal fluorescence projection images (Fig. 2B) for each

position in the samples using the z-stack function in Fiji. The MIP was applied only along the optical axis, where the oxygen concentration is assumed to be uniform within the cuvette height. This approach ensured that the brightest focal plane of each bead (centre) was captured. Three-dimensional oxygen variation was assessed by translating the sample laterally (*Y*-axis), thereby enabling depth-dependent oxygen measurements. Representative images from different stages of the processing pipeline are shown in Fig. 2. Beads were segmented from the background using manual thresholding in MATLAB (Mathworks, USA) (Fig. 2D). For each MIP image, the background fluorescence intensity was determined by measuring the highest intensity value adjacent to the beads using Fiji. To further remove high-intensity artefacts, values above calibrated mean bead intensity (+ standard deviation) at 0% oxygen were also removed from the MIP images in MATLAB. For bead size quantification and subsequent conversion of intensity values into oxygen concentration, binary thresholding was applied to create a binary mask. Following this, connected component analysis (using 8-connectivity) was performed on the binary mask to identify and label individual beads. Each connected object was treated as a separate bead and analysed individually. The diameter of each bead was then quantified and beads smaller than 45 μm (cut-off) in diameter were filtered out from the analysis to remove debris and partial detections. The selected size range was consistent with the manufacturer-reported average bead diameter of approximately 50 μm, considering expected size variability. Beads outside the defined size range were not included in the quantitative analysis. Within this selected size range, a sufficient number of beads were distributed throughout the image to ensure reliable averaging for the retained beads (Fig. 2E). The intensity values were converted to oxygen concentration using a simplified linear Stern–Volmer
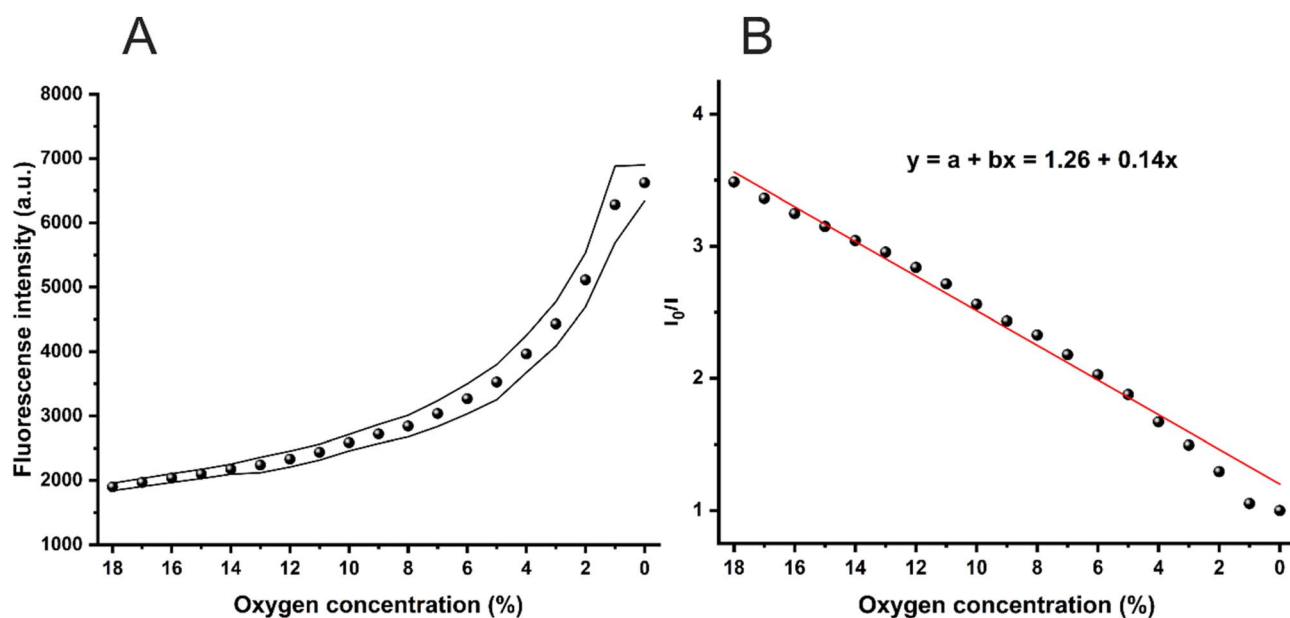

Fig. 4 Calibration curve for CPOx-50-PtP beads at different oxygen concentrations. (A) Mean intensity data acquired from the calibration measurement plotted with an error band showing the standard deviation ($n = 5$). Decreasing oxygen concentration is shown on the *x*-axis and fluorescence intensity on the *y*-axis. (B) Relationship between O_2 concentration and fluorescence intensity after calibration: intensity ratios plotted by dividing the highest mean intensity (I_0) by the mean intensity (I) at each oxygen concentration level. Linear fit shown in red.

model derived from calibration experiments. Analysis was performed on multiple segmented probes within each field of view to reduce the influence of local intensity fluctuations and improve the robustness of the oxygen mapping. This conversion was implemented in Python within an Anaconda environment. The results were visualized using the Fire colormap in Fiji, and the mean and standard deviation of the oxygen values were calculated and plotted. For quantitative comparison across different cell culture conditions, including variations in cell density and imaging depth, oxygen concentrations were extracted from individual microsensor beads and averaged over all probes detected within the field of view at each depth, with values reported as mean $\pm$ standard deviation. The measurements were validated by measuring oxygen concentrations with the PM-PSt7 optical fibre sensor near the centre of each field of view after the whole sample had been imaged.

3. Results

3.1. Photostability of CPOx-50-PtP microsensor beads

To ensure the stability and reliability of oxygen measurement using the CPOx-50-PtP beads, a photobleaching experiment was performed using the MF-OPM system. Fluorescence intensity was recorded for a duration of 120 minutes by measuring a 10×10 pixel region at the centre of individual microbeads. The intensity remained stable throughout the measurement period, as shown in Fig. 3, indicating no significant photobleaching. The differences in intensities between the beads reflect spatial variation within the beads rather than temporal signal decay, as further shown in SI Fig. S1. These findings confirm the photostability of the sensor beads under the applied imaging settings.
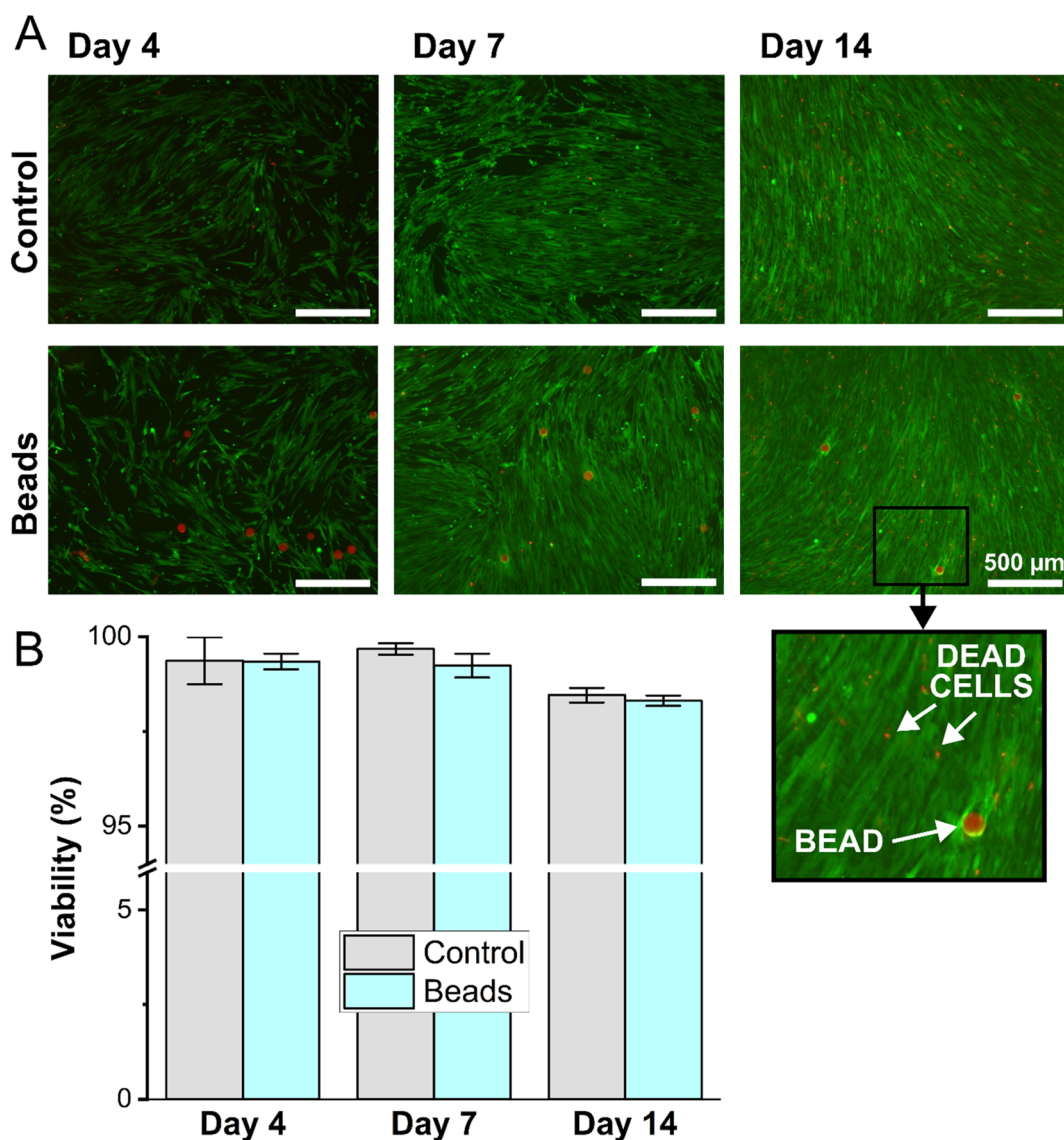

Fig. 5 (A) Representative viability test micrographs and (B) viability percentage calculations show good viability for the WI-38 fibroblast cells in all samples during the 2-week culture. In (A) live cells are shown in green and dead in red. Scale bars indicate 500 μm. The chart (B) shows mean viability percentages and standard deviation. $N = 4$.

3.2. Calibration curve for oxygen concentration measurements

To measure oxygen levels in the 3D sample using MF-OPM, a calibration curve was established by correlating the fluorescence intensity of CPOx-50-PtP beads with oxygen concentration measured using the PM-PSt7 optical fibre probe. The relationship between mean fluorescence intensity and oxygen level, along with the associated standard deviations, is shown in Fig. 4. At low oxygen levels (0–4%), the fluorescence intensity changed more noticeably, indicating higher sensitivity under hypoxic conditions. In contrast, higher oxygen values exhibited small intensity differences and lower sensitivity, though with relatively larger standard deviations. The calibration data were fitted to a linear model based on the Stern–Volmer equation (eqn (1)), where the ratio I_0/I showed a clear linear relationship with oxygen concentration. The parameters of the fitted model are shown in Fig. 4B. These results demonstrate the suitability of the Stern–Volmer model for converting fluorescence intensity into oxygen concentration in the subsequent measurements.

3.3. CPOx-50-PtP microsensor bead cytocompatibility

Based on visual observation, the fibroblasts started to show their normal elongated shape after 24 hours in culture during the first inspection after plating. Cell confluency changed from approximately 50% to 100% in 10 days, indicating good cell proliferation. Viability was high in all the samples and all the controls in the cell culture experiment as shown in Fig. 5. Calculated viability percentage was above 98% (98.5 ± 0.2%) at all points and standard deviation did not exceed 0.6%. These results show good cytocompatibility for the microsensor beads, which have also been previously successfully used in cell culture experiments.[31,32]

3.4. Oxygen concentration measurements in large volume 3D hydrogel cell cultures

Across all samples, oxygen concentration decreased with increasing depth as shown in oxygen maps in Fig. 6. Some variation in oxygen levels can be observed within each image. Because the image area is relatively large, slight differences in local oxygen concentration were expected. Some outlier beads, caused by non-uniform coating (SI Fig. S1), led to localized oxygen values exceeding the normoxic level (Fig. 6). However, these variations have insignificant effect on the overall mean oxygen values. Fig. 7 presents the mean oxygen concentration plot with standard deviations at each measured position. The results show that both higher cell density and deeper imaging depth contribute to lower oxygen availability, resulting in a steep oxygen gradient throughout the samples. Specifically, for 200 000 cells per ml, oxygen concentration decreased from 20.8% near the medium surface to 15.3% at the bottom of the sample. At 400 000 cells per ml and 700 000 cells per ml, the decreases were from 16.8% to 8.0% and from 12.0% to 2.5%, respectively. As expected, the change in oxygen concentration was most significant at the highest cell density (700 000 cells per

ml), indicating the greater oxygen consumption associated with increased cell numbers. Although bead distributions were not perfectly uniform (Fig. 6) at higher densities, the oxygen values in Fig. 7 represent averages over multiple probes within the field of view, accounting for local heterogeneity. Live/dead staining showed mostly viable cells with rounded morphology consistent with a 3D culture state throughout the samples (Fig. S2). Overall, these results highlight the suitability of the developed oxygen imaging method for assessing depth-dependent oxygen gradients in 3D cell cultures. Validation measurements using a fibre-optic sensor at eight depths within the cultures, with pointwise measurements performed near the centre of the corresponding MF-OPM field of view, showed acceptable statistical agreement (Table S1).
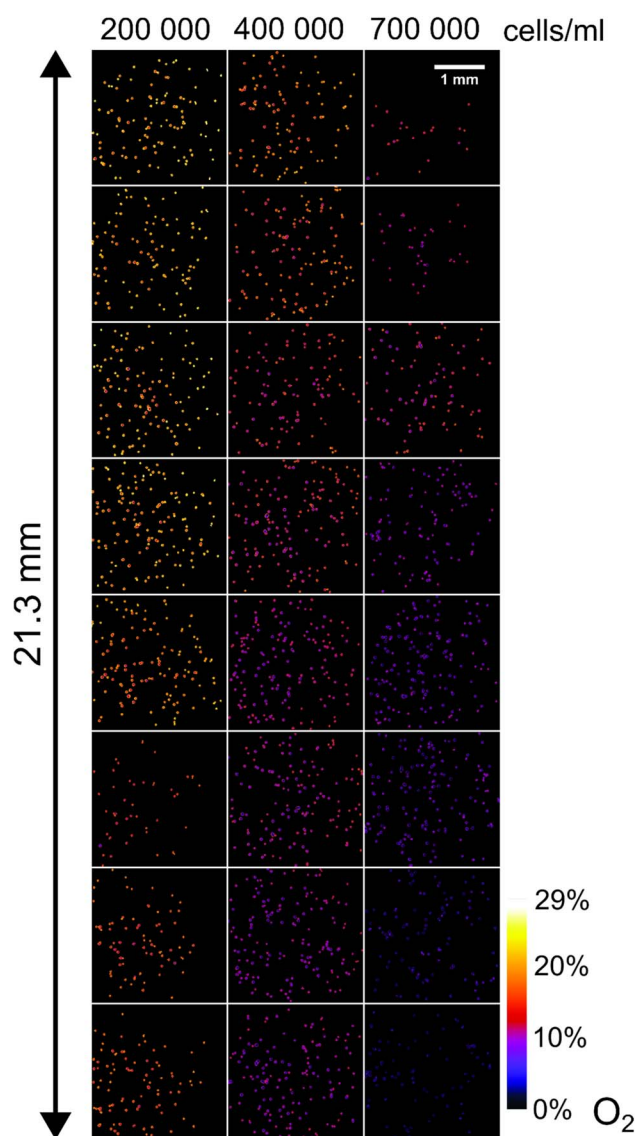

Fig. 6 O$_2$ levels in fibroblast 3D cell cultures with oxygen sensitive beads shown as an intensity color map after 48 hours of incubation. The results show that oxygen concentration is affected by cell density and measurement depth. The scale bar indicates 1 mm.

4. Discussion

We developed a quantitative measurement method and a protocol utilizing multifocal optical projection microscopy[27] (MF-OPM) combined with oxygen sensitive fluorescent microsensor beads and oxygen level calibration to measure oxygen concentration in large volume hydrogel-based 3D cell cultures. This robust approach allowed us to assess the oxygen concentrations and here we demonstrated the minimally invasive method at depths up to 21 mm and across different densities of fibroblasts within agarose hydrogel. The multifocal imaging capabilities of the system enabled rapid acquisition of images from different focal planes, providing 2D visuals of the culture. The presence of oxygen molecules reversibly quenches the fluorescence signal from the sensor beads. This allowed us to calibrate the sensor beads' fluorescence intensity with oxygen concentration, and to successfully quantify oxygen concentrations and their gradients in our samples. We demonstrated the capability of the method by showing that oxygen concentrations decrease with both increasing cell density and increasing distance from the oxygen source.

To ensure the reliability of intensity-based oxygen measurement, we first characterized the photostability and cytocompatibility of microsensor beads. The beads exhibited minimal photobleaching during the 120-minute imaging experiment. The fibroblast cells were viable above 98% at all time-points during the two-week culture period. Live/dead staining was used to briefly inspect cell viability in the 3D cultures. The rounded cell morphology reflects the bioinert nature of agarose and supports that fibroblasts are cultured in a true 3D environment. The number of live cells in each sample was sufficient to create oxygen concentration gradients needed to demonstrate our method. Previous publications demonstrating the use of microsensor beads to study cell cultures[13,33,34] further support the suitability of their use for monitoring oxygen concentrations in cell cultures. These results collectively demonstrate that the microsensor bead approach is reliable and cytocompatible for oxygen measurement in *in vitro* 3D cell culture environments. Also, they demonstrate the need for such methods in 3D cell cultures as the oxygen is consumed by the cells, possibly resulting in oxygen deprivation and unwanted ischemic conditions.

Quantification of oxygen concentration from sensor beads' fluorescence intensity required generation of a calibration curve. To this end, we established a Stern–Volmer relationship using sodium sulfate as an oxygen quencher. The changes in fluorescence intensity were largest in the 0–6% oxygen range, indicating that the method is most sensitive at low oxygen concentrations. On the other hand, the standard deviation in the 6–18% oxygen range was lower, which enhances the accuracy of measurements in that range. These calibration results show that the sensor bead-based method provides high sensitivity at low oxygen concentration and improved accuracy at higher concentrations. This makes the developed method suitable for characterizing physioxic, hypoxic and anoxic conditions *in vitro* 3D cultures.

In the fluorescence-intensity-based oxygen sensing, variations in imaging focus can significantly affect the measured intensity values, especially when using relatively large sensor beads such as in this work with a 50-micron diameter. Since fluorescence intensity directly influences oxygen quantification, such variability could lead to incorrect interpretation of spatial oxygen distribution. To address this, our protocol incorporates multifocal imaging using an electrically tunable lens (ETL), which allows rapid and precise focus scanning.[35,36] As demonstrated in our previous work, an applied current to the ETL produces a linear shift in focal position.[27] By acquiring multiple focal planes and computing maximum intensity projection (MIP) images, we minimized focus-related signal variations and ensured a more consistent representation of bead fluorescence. These MIP images were then converted into oxygen concentration maps using the Stern–Volmer calibration curve.

To further validate the oxygen measurement protocol and investigate how cell density and depth influence oxygen availability, fibroblasts were cultured at 200 000–700 000 cells per ml within 3D agarose hydrogels and imaged using the MF-OPM system. Although a 21 mm measurement depth exceeds the typical 3D culture dimensions, we demonstrated that our system enabled the evaluation of oxygen concentration gradients throughout the relatively large samples. After 48 hours of culture, the cellular oxygen consumption resulted in decreasing oxygen concentrations with both increasing cell density and depth of the specimen. At the lowest cell density, oxygen dropped by approximately 26% from top to bottom. In the medium- and high-density cultures, the relative decreases were even more pronounced, at around 52% and 79%, respectively. Of the 24 measured positions, 9 fell outside the broad physioxic range (1.1–13.5%),[1,2] and only two were within 1% of the 5.6% oxygen concentrations typical for human lung fibroblasts *in vivo*.[37] These comparisons emphasize how much variation these cells experience regarding surrounding oxygen concentration. In addition, pointwise measurements performed near the centre of the corresponding MF-OPM field of view using the PM-PSt7 fibre-optic sensor showed acceptable statistical agreement, further supporting the accuracy of the approach. These findings also align with the previous studies on oxygen availability in hydrogel-based 3D cell cultures,[5–7,9] confirming that higher cell density results in increased oxygen consumption, which limits diffusion and accelerates oxygen depletion. Importantly, the developed method effectively detected these gradients, demonstrating its sensitivity and suitability for oxygen quantification in 3D culture.

Although useful, the cell densities used here are relatively low compared to those in human tissues (1–3 billion cells per ml),[38] or typical tissue-engineered constructs (few million cells per ml to few hundred million cells per ml).[39] However, densities below 1 million cells per ml have been previously used with these fibroblasts.[40] Additionally, oxygen consumption rate varies across cell types[41] and culture approaches like spheroids and organoids,[42] which further affects oxygen availability. At higher densities and cellular oxygen consumption rates as in the case of neuronal cells and myocytes, the risk of hypoxia increases without adequate perfusion or vascularization. It can
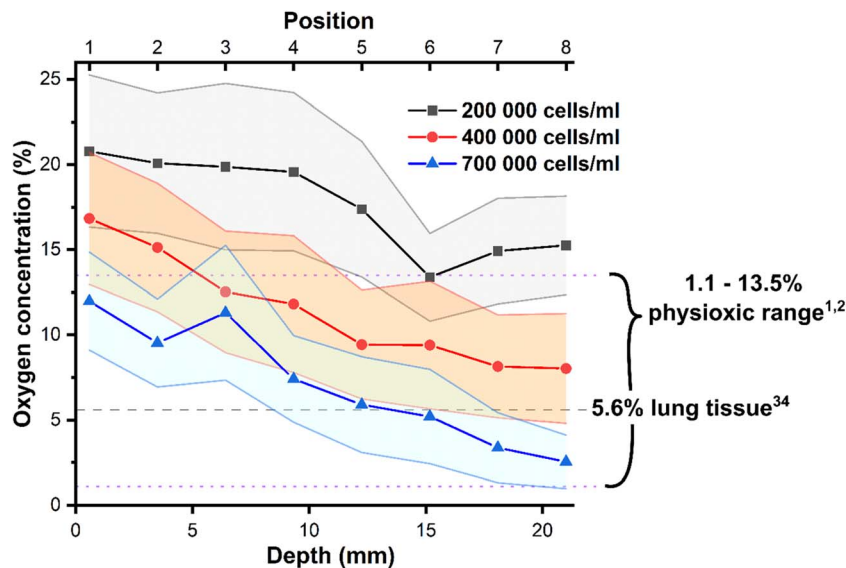
Fig. 7 O_2 concentration in fibroblast 3D cell cultures shown as a line graph after 48 hours of incubation. The mean intensities from each position are presented with standard deviation shown as error bands. Oxygen concentration can be seen to decrease together with increased depth and cell density. Only half of the measured positions were within the physioxic range.

be advantageous when modelling, for example pre-vascular development,[43] cancer[44] or hypoxic disease[3] in tissues, but it can be a serious problem when modelling healthy tissues.[45] These results show the need to carefully consider cell density, oxygen delivery, and model design in 3D culture systems.

A key limitation of intensity-based oxygen measurement with microsensor beads is its sensitivity to factors such as variations in bead size and non-uniform oxygen-sensitive coating. These introduce inconsistencies in fluorescence signals, reducing the reliability of localized oxygen measurements. As a result, the method is more suitable for estimating average oxygen concentration across a region rather than precise, bead-level accuracy. This limitation is evident in the relatively high standard deviation in the calibration curve, especially at low oxygen concentrations and in the presence of high intensity individual pixels corresponding to an oxygen concentration of 29% in the oxygen map (Fig. 6). In addition, as an intensity-based approach, oxygen quantification is referenced to defined experimental conditions and may require generation of a new calibration curve under different optical settings or gel compositions. The method relies on commercially available oxygen-sensitive beads, fluorescence imaging and quantitative analysis and is therefore not restricted to a specific biological model or device. This study demonstrates reliable performance under controlled conditions. However, broader validation across different devices and biological samples remains an important direction for future work. While more accurate quantification could be achieved using luminescence lifetime methods,[13] such approaches typically require advanced instrumentation, which are complex and costly. However, since lifetime measurements are independent of signal intensity, the influence of artifacts caused by bead size and coating variability is minimal. Further advances in the development of commercially available sensor beads with uniform fluorescence

properties would improve the accuracy and reproducibility of intensity-based oxygen measurement. However, even if our method may not be the best to assess the environment of single cells, it shows promise in assessing the entire cell culture and the dependence of O_2 availability on cell density and depth.

Our method complements existing approaches by allowing measurements from the entire large-volume samples, facilitated by the relatively uniform spatial distribution of sensor beads. Its use, however, depends on sample transparency, as the beads must be optically excited and imaged using fluorescence microscopy. Optical fibre measurements[6,15–17] do not require transparent samples but are invasive and limited to single point detection. In contrast, after calibrating with dedicated samples, our measurements can be performed without further disturbing the sample by inserting a probe. Averaging intensities across multiple beads reduce spatial resolution but minimize the influence of local variations within the sample volume. Peripheral oxygen measurements[9,18–21] avoid the need for sample transparency but lack direct measurements from most of the volume. Other volumetric approaches rely on dispersed beads[13,22,23,31] or a stationary ramp[46] and are commonly based on ratiometric[22,24,46] and PLIM[13,23,31] imaging. These methods offer more accurate measurements with higher spatial resolution but typically require custom-made sensors or specialized instrumentation. Our approach, which uses commercially available sensor beads and allows relatively larger sample dimensions, provides a practical and versatile alternative to existing tools. While fibre-based and other 1D methods[9,20,47] allow continuous real-time monitoring at a single point, our method enables spatial mapping of oxygen gradients within the sample. Although measurements are acquired at discrete time points and require post-processing, several of the previously mentioned methods are also capable of 2D and 3D time-dependent measurements from sample interiors.[13,22,24,46]

To summarize, MF-OPM and fluorescent oxygen sensing beads after calibration enable reliable estimation of molecular oxygen concentrations in large-volume hydrogel-based 3D cell cultures. We successfully demonstrated the novel method's capability to detect the expected relationship between cell density, measurement depth, oxygen concentrations, and oxygen gradients. Given the commercial availability of the beads and the established analysis method, they can be adapted for use with MF-OPM. The reversible oxygen binding of the beads allows for monitoring dynamic changes in oxygen levels. Combined with environmental control and the method's minimal invasiveness, this approach has the potential for online measurements during long-term cell culture experiments with further development. The protocol is also compatible with both in-house and commercial fluorescence systems, including wide-field and confocal fluorescence microscopy. In addition to strong applications in 3D cell culture, it also offers a potential tool for quantifying oxygen in complex systems such as organoid cultures and tissue engineering constructs.

5. Conclusions

In this work, we developed an optical method for estimating oxygen concentrations in large-volume hydrogel-based 3D cell cultures using the MF-OPM system. We have successfully demonstrated the method's capability to quantify oxygen levels and gradients across varying cell densities and depths with minimal invasiveness. This approach can provide valuable support for development, monitoring, and validation of 3D cell culture models. Accurate control and measurement of oxygen availability are crucial not only for mimicking physiological conditions but also for modelling disease states such as ischemic stroke or cardiac ischemia. Together with its minimal invasiveness nature and straightforward implementation, the method can be adapted for routine use with wide-field fluorescence microscopy systems.

Author contributions

B. Belay, M. Kroon, J. Hyttinen and M. Kellomäki contributed to the design of the study. B. Belay was responsible for MF-OPM development and imaging and M. Kroon the cell culturing experiment. B. Belay and M. Kroon developed the oxygen measurement technique, analysed image datasets and wrote the manuscript. K. Walls contributed to cell culturing and imaging. All authors contributed to the drafting and reviewing of the manuscript. All authors have approved the submitted version.

Conflicts of interest

The authors declare no competing interests.

Data availability

The data that support the findings of this study are available from the corresponding author upon request.

References

1 W. Wang, C. P. Winlove and C. C. Michel, *J. Physiol.*, 2003, **549**, 855–863.
2 S. R. McKeown, *Br. J. Radiol.*, 2014, **87**, 20130676.
3 M. Häkli, J. Kreutzer, A.-J. Mäki, H. Välimäki, H. Lappi, H. Huhtala, P. Kallio, K. Aalto-Setälä and M. Pekkanen-Mattila, *Sci. Rep.*, 2021, **11**, 4153.
4 P. M. Holloway and F. N. E. Gavins, *Stroke*, 2016, **47**, 561–569.
5 K. Duval, H. Grover, L.-H. Han, Y. Mou, A. F. Pegoraro, J. Fredberg and Z. Chen, *Physiology*, 2017, **32**, 266–277.
6 L. Figueiredo, R. Pace, C. D'Arros, G. Réthoré, J. Guicheux, C. Le Visage and P. Weiss, *J. Tissue Eng. Regen. Med.*, 2018, **12**, 1238–1246.
7 I. Streeter and U. Cheema, *Analyst*, 2011, **136**, 4013–4019.
8 A. P. Van Winkle, I. D. Gates and M. S. Kallos, *Cells Tissues Organs*, 2012, **196**, 34–47.
9 H. Zirath, M. Rothbauer, S. Spitz, B. Bachmann, C. Jordan, B. Müller, J. Ehgartner, E. Priglinger, S. Mühleder, H. Redl, W. Holnthoner, M. Harasek, T. Mayr and P. Ertl, *Front. Physiol.*, 2018, **9**, 815.
10 N. B. Schack, C. L. P. Oliveira, N. W. G. Young, J. S. Pedersen and P. R. Ogilby, *Langmuir*, 2009, **25**, 1148–1153.
11 H. Vuorenpää, M. Björninen, H. Välimäki, A. Ahola, M. Kroon, L. Honkamäki, J. T. Koivumäki, M. Pekkanen-Mattila, *et al.*, *Frontiers in Physiology*, 2023, **14**, 1213959.
12 L. Ouyang, J. P. K. Armstrong, Q. Chen, Y. Lin and M. M. Stevens, *Adv. Funct. Mater.*, 2020, **30**, 1908349.
13 M. F. Wesseler, M. N. Johansen, A. Kızıltay, K. I. Mortensen and N. B. Larsen, *Lab Chip*, 2022, **22**, 4167–4179.
14 S. M. Mavris and L. M. Hansen, *J. Biomech. Eng.*, 2021, **143**, 101004.
15 S. Eggert, M. S. Gutbrod, G. Liebsch, R. Meier, C. Meinert and D. W. Hutmacher, *ACS Sens.*, 2021, **6**, 1248–1260.
16 L. Figueiredo, C. Le Visage, P. Weiss and J. Yang, *Polymers*, 2020, **12**, 1260.
17 P. Wolff, L. Heimann, G. Liebsch, R. J. Meier, M. Gutbrod, M. van Griensven and E. R. Balmayor, *Mater. Sci. Eng. C*, 2019, **95**, 422–427.
18 M. W. Boyce, W. C. Simke, R. M. Kenney and M. R. Lockett, *Anal. Methods*, 2019, **12**, 18–24.
19 H. Välimäki, K. Ameziane, S. Bhattacharya, J. Massera, P. Kallio and J. N. Anker, *ACS Biomater. Sci. Eng.*, 2025, **11**, 4050–4056.

20 C. Schmitz, I. Pepelanova, C. Ude and A. Lavrentieva, *J. Tissue Eng. Regen. Med.*, 2022, **16**, 977–986.

21 S. C. Lesher-Pérez, G.-A. Kim, C. Kuo, B. M. Leung, S. Mong, T. Kojima, C. Moraes, M. D. Thouless, G. D. Luker and S. Takayama, *Biomater. Sci.*, 2017, **5**, 2106–2113.

22 R. L. Wilson, J. P. Connell and K. J. Grande-Allen, *ACS Biomater. Sci. Eng.*, 2019, **5**, 4522–4530.

23 X. Mei, Q. Fang and P. R. Selvaganapathy, *Biomed. Opt. Express*, 2023, **14**, 4759–4774.

24 D.-M. Chang, H.-H. Hsu, P.-L. Ko, W.-J. Chang, T.-H. Hsieh, H.-M. Wu and Y.-C. Tung, *Analyst*, 2024, **149**, 1727–1737.

25 W. Becker, *J. Microsc.*, 2012, **247**, 119–136.

26 R. Datta, T. M. Heaster, J. T. Sharick, A. A. Gillette and M. C. Skala, *J. Biomed. Opt.*, 2020, **25**, 1–43.

27 B. Belay, E. Figueiras, J. Hyttinen and A. Ahola, *Sci. Rep.*, 2023, **13**, 19788.

28 B. Belay, J. T. Koivisto, J. Parraga, O. Koskela, T. Montonen, M. Kellomäki, E. Figueiras and J. Hyttinen, *Sci. Rep.*, 2021, **11**, 6538.

29 J. Schindelin, I. Arganda-Carreras, E. Frise, V. Kaynig, M. Longair, T. Pietzsch, S. Preibisch, C. Rueden, S. Saalfeld, B. Schmid, J.-Y. Tinevez, D. J. White, V. Hartenstein, K. Eliceiri, P. Tomancak and A. Cardona, *Nat. Methods*, 2012, **9**, 676–682.

30 R. F. Place, E. J. Noonan and C. Giardina, *BMC Cell Biol.*, 2005, **6**, 37.

31 M. F. Wesseler, N. Taebnia, S. Harrison, S. Youhanna, L. C. Preiss, A. M. Kemas, A. Vegvari, J. Mokry, G. J. Sullivan, V. M. Lauschke and N. B. Larsen, *Acta Biomater.*, 2023, **171**, 336–349.

32 D. Bavli, S. Prill, E. Ezra, G. Levy, M. Cohen, M. Vinken, J. Vanfleteren, M. Jaeger and Y. Nahmias, *Proc. Natl. Acad. Sci. U. S. A.*, 2016, **113**, E2231–E2240.

33 M. F. Wesseler, N. Taebnia, S. Harrison, S. Youhanna, L. C. Preiss, A. M. Kemas, A. Vegvari, J. Mokry, G. J. Sullivan, V. M. Lauschke and N. B. Larsen, *Acta Biomater.*, 2023, **171**, 336–349.

34 B. Weyand, M. Nöhre, E. Schmälzlin, M. Stolz, M. Israelowitz, C. Gille, H. P. von Schroeder, K. Reimers and P. M. Vogt, *Biores. Open Access*, 2015, **4**, 266–277.

35 L. Chen, S. Kumar, D. Kelly, N. Andrews, M. J. Dallman, P. M. W. French and J. McGinty, *Biomed. Opt. Express*, 2014, **5**, 3367–3375.

36 F. O. Fahrbach, F. F. Voigt, B. Schmid, F. Helmchen and J. Huisken, *Opt. Express*, 2013, **21**, 21010–21026.

37 Q.-T. Le, E. Chen, A. Salim, H. Cao, C. S. Kong, R. Whyte, J. Donington, W. Cannon, H. Wakelee, R. Tibshirani, J. D. Mitchell, D. Richardson, K. J. O'Byrne, A. C. Koong and A. J. Giaccia, *Clin. Cancer Res.*, 2006, **12**, 1507–1514.

38 J. Bronzino, J. Enderle and S. M. Blanchard, in *Introduction to Biomedical Engineering*, Elsevier Science & Technology, United States, 2005.

39 M. A. Skylar-Scott, S. G. M. Uzel, L. L. Nam, J. H. Ahrens, R. L. Truby, S. Damaraju and J. A. Lewis, *Sci. Adv.*, 2019, **5**, eaaw2459.

40 C. Gering, J. T. Koivisto, J. Parraga, J. Leppiniemi, K. Vuornos, V. P. Hytönen, S. Miettinen and M. Kellomäki, *PLoS One*, 2019, **14**, e0221931.

41 B. A. Wagner, S. Venkataraman and G. R. Buettner, *Free Radicals Biol. Med.*, 2011, **51**, 700–712.

42 H. M. Tse, G. Gardner, J. Dominguez-Bendala and C. A. Fraker, *Front. Bioeng. Biotechnol.*, 2021, **9**, 634403.

43 M. C. Simon and B. Keith, *Nat. Rev. Mol. Cell Biol.*, 2008, **9**, 285–296.

44 F. Moradi, C. Moffatt and J. A. Stuart, *Biomolecules*, 2021, **11**, 1177.

45 T. L. Place, F. E. Domann and A. J. Case, *Free Radicals Biol. Med.*, 2017, **113**, 311–322.

46 C. J. Peniche Silva, G. Liebsch, R. J. Meier, M. S. Gutbrod, E. R. Balmayor and M. van Griensven, *Front. Bioeng. Biotechnol.*, 2020, **8**, 595.

47 S. Kreß, R. Schaller-Ammann, J. Feiel, J. Wegener, J. Priedl, W. Dietrich, C. Kasper and D. Egger, *Cells*, 2022, **11**, 412.